Pattern Recognition 172 (2026) 112694

Contents lists available at ScienceDirect

Pattern Recognition

journal homepage: www.elsevier.com/locate/pr

Restoration of partially damaged fingerprints using a partial differential equation

Sangkwon Kim [a], Yibao Li [b], Soobin Kwak [a], Junseok Kim [a,*]

[a] Department of Mathematics, Korea University, 02841, Seoul, Republic of Korea
[b] School of Mathematics and Statistics, Xi'an Jiaotong University, 710049, Xi'an, China

ARTICLE INFO

Keywords:
Damaged fingerprint
Partial differential equation
Sweeping ordering
Finite difference method
Isotropic Laplacian operator

ABSTRACT

We present novel sweeping ordering algorithms for the restoration of partially damaged fingerprint images using a partial differential equation (PDE). To efficiently and numerically solve the PDE in the discretized domain, we use the proposed sweeping ordering algorithm in conjunction with a Gauss–Seidel-type update method and an isotropic Laplacian operator. To achieve accurate and stable restoration, we use the information surrounding the damaged region as Dirichlet boundary conditions and propose a method to match the amplitude and wavelength of the damaged fingerprint image with the numerical solution. The proposed sweeping ordering algorithm starts at an interior point adjacent to a boundary point and spirals inward from this point. In this process, it visits all interior points progressively.

1. Introduction

Fingerprint recognition is regarded as one of the most dependable and extensively adopted biometric authentication technologies in various fields, including civil identification, forensic investigations, and commercial security systems [1]. Due to their unique and immutable characteristics, fingerprints provide the advantage of low implementation and processing costs. These benefits have made fingerprint authentication a widely accepted and popular choice for security applications. Although other biometric technologies, such as iris, palm, and face recognition, along with hybrid systems, have advanced, their adoption is primarily dependent on cost-effectiveness. Recently, machine learning and deep learning technologies have demonstrated excellent performance in the image processing field, playing a significant role in security applications such as facial recognition and fingerprint authentication. However, despite the robustness of fingerprint recognition systems, their accuracy heavily relies on the quality of the input fingerprint images. In real-world scenarios, fingerprint images are often compromised by imperfections such as low contrast, blurred ridge patterns, scratches, fractures, or occlusions. To improve ridge continuity and minimize incorrect or redundant minutiae, it is crucial to reconstruct degraded fingerprint images, especially those with low contrast and poorly defined ridge boundaries [2,3].

Fingerprints exhibit diverse structural patterns, generally classified into three major categories: loops, whorls, and arches. Loops are the most common, characterized by ridges that enter and exit on the same side of the finger. Whorls display circular or spiral-like patterns, while arches are simpler, with ridges flowing continuously from one side to the other without looping. The variations in these patterns, combined with individual-specific minutiae points, make fingerprints unique. However, the diversity in fingerprint patterns also poses a challenge for restoration techniques, as different patterns may require tailored algorithms to reconstruct ridge structures accurately.

The types of damage that affect fingerprint images can vary widely depending on the acquisition process, environmental conditions, and physical handling. Common forms of damage include scratches, smudges, and partial obliteration of ridge patterns. For example, ridge modeling approaches have used contextual information to restore intricate ridge structures lost in damaged areas [4]. A trustworthy and stable method has been proposed to resolve the challenges in fingerprint recognition caused by geometric distortions by using a novel feature, the Middle of the Triangle's Side (MTS), derived from minutiae triangles [5]. The method resolves various uncertainty factors in fingerprint image quality, enabling the rapid detection and removal of low-quality images to ensure that AFIS processes only high-quality ones [6]. These innovative methods highlight the adaptability of advanced restoration techniques to various types of fingerprint damage.

Recent machine learning techniques have introduced diverse methods for restoring damaged fingerprint images. For example, machine learning-based algorithms, such as convolutional neural networks (CNNs) [7–11] and generative adversarial networks (GANs) [12–14], have demonstrated remarkable success in fingerprint restoration tasks.

* Corresponding author.
E-mail addresses: ksk8863@korea.ac.kr (S. Kim), yibaoli@xjtu.edu.cn (Y. Li), soobin23@korea.ac.kr (S. Kwak), cfdkim@korea.ac.kr (J. Kim).

https://doi.org/10.1016/j.patcog.2025.112694
Received 14 May 2025; Received in revised form 10 September 2025; Accepted 30 October 2025
Available online 20 November 2025

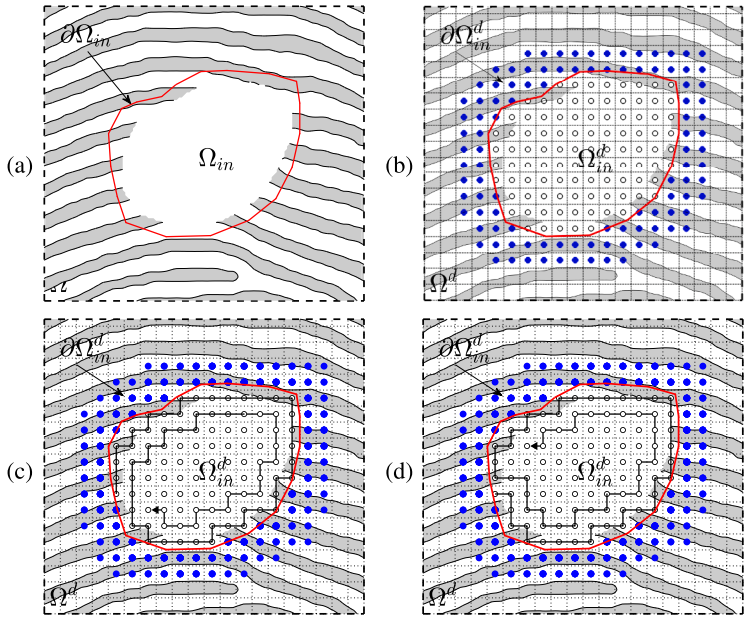

Fig. 1. (a) User-selected damaged domain Ω_{in} with boundary $\partial\Omega_{in}$ in the whole domain Ω. (b) Discretized domains: user-selected damaged discrete domain Ω^d_{in} (open circles) with discrete boundary $\partial\Omega^d_{in}$ (filled circles) in the whole discrete domain Ω^d. (c) Clockwise sweeping ordering for updating the numerical solution. (d) Counterclockwise sweeping ordering for updating the computational solution.

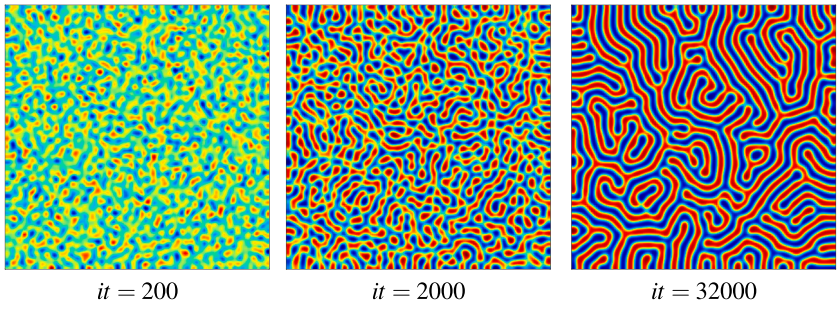

Fig. 2. Temporal evolution results of the nonlocal CH with the lamellar phase.

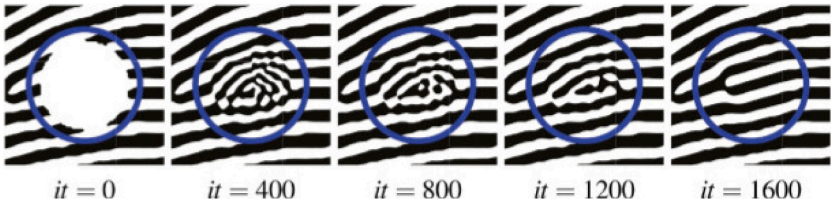

Fig. 3. The schematic illustration of fingerprint image restoration mechanism. Reprinted from [25], with permission from Elsevier.

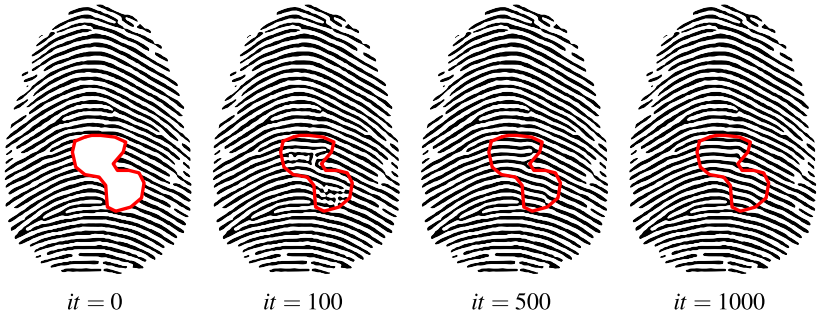

Fig. 4. Temporal progression of the damaged fingerprint image within the user-defined domain across various iterations (it). From left to right, the specified iterations are $it = 0,\ 100,\ 500$, and 1000. Modified from [25], with permission from Elsevier.

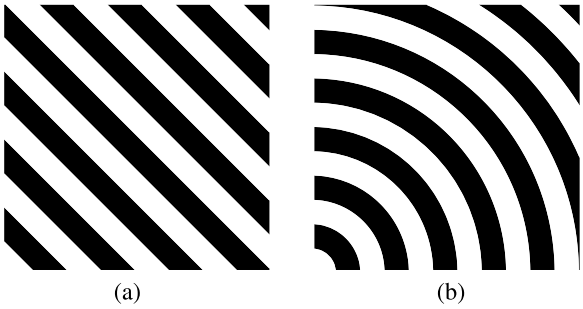

Fig. 5. Contour plots generated for the synthetic pattern images of (a) $\hat{f}_1$ and (b) $\hat{f}_2$.

Advanced methods, such as Unet-based models for segmenting and reconstructing latent fingerprints, have further enhanced the ability to recover fine details from noisy and incomplete images [15]. Furthermore, Pix2Pix conditional generative adversarial networks (cGANs) have been used to reconstruct degraded regions and achieve high restoration accuracy by leveraging triplet loss functions [16]. The KNN-SVD based method [17] restores damaged fingerprint regions through similar patch matching and singular value refinement, and shows potential for improving recognition performance even on degraded fingerprints.

In addition to machine learning techniques, mathematical models have provided a robust framework for resolving fingerprint restoration problems. Partial differential equations (PDEs) have gained attention for their ability to model complex restoration tasks by considering local and nonlocal properties of the image. The phase-field model has gained prominence for its ability to model complex restoration tasks by incorporating both local and nonlocal properties of the image. These models have been extensively applied in various image processing tasks, including image segmentation [18], shape transformation [19], and inpainting [20,21]. Furthermore, active research has been conducted to develop efficient numerical methods and to apply extensions of the model, broadening its applicability to various contexts [22–24]. Li et al. developed an efficient method for fingerprint restoration using a nonlocal Cahn–Hilliard (CH) equation, which demonstrated excellent performance in reconstructing ridge patterns and maintaining smooth transitions across damaged regions [25]. Similarly, Lee et al. developed a semi-automatic method using the CH equation with a source term. The method minimizes user intervention by automatically determining the necessary parameter values, thereby simplifying the restoration procedure [26].

The purpose of our research is to present novel sweeping ordering algorithms for restoring partially damaged fingerprint images using a PDE. Unlike machine learning and deep learning-based methods, the proposed method does not require extensive training on large-scale fingerprint datasets. It uses only local information adjacent to the corrupted regions within a single image, instead of using the entire image. This method aims to overcome inherent limitations of conventional fingerprint restoration techniques, in particular, the directional bias often found in Gauss-Seidel-type iterative schemes. This bias is caused by fixed traversal patterns during the numerical update process and results in uneven propagation of corrections throughout the computational domain. To mitigate this issue, our study introduces two significant improvements: the application of an isotropic Laplacian operator and a spiral sweeping ordering algorithm. The isotropic Laplacian operator ensures rotational invariance and minimizes numerical anisotropy, enabling accurate solutions regardless of the computational domain's orientation. Meanwhile, the spiral sweeping ordering method eliminates directional dependence by alternating between clockwise and counterclockwise updates, and this approach ensures that the restoration process remains balanced. Additionally, we tackle the challenge of scale mismatch between the damaged fingerprint image and the numerical solution derived from the governing equation. Such a discrepancy may compromise the accuracy of restoration if it is not properly resolved. To resolve this, our approach incorporates a novel image-scaling parameter that is determined based on the numerical solution's amplitude. This incorporation enables consistent and reliable restoration performance across varying damage levels and image properties. Through these advancements, our work aims to present a robust method for fingerprint restoration and to improve both computational efficiency and the fidelity of reconstructed patterns.

The structure of the article is outlined as follows. Section 2 describes the proposed sweeping technique, along with its enhancements for fingerprint restoration. Section 3 presents numerical tests designed to validate the efficiency of the proposed method. Lastly, Section 4 concludes the paper.

2. Proposed numerical algorithm

The proposed numerical algorithm restores damaged fingerprint images by solving the nonlocal CH equation using an efficient sweeping ordering scheme. For a 2D image representation, let Ω_{in} represent the user-defined damaged region within the rectangular domain Ω, and let $\partial\Omega_{in}$ denote the boundary of Ω_{in}; see Fig. 1(a). Let $f(\mathbf{x})$ be a given grayscale fingerprint image. Typically, grayscale digital image data consist of pixels whose values range from 0 to 255. To transform the grayscale image into the computational framework, $f(\mathbf{x})$ is scaled as follows:

$$\bar{f}(\mathbf{x}) = \beta\left(\frac{2f(\mathbf{x}) - f_{\min} - f_{\max}}{f_{\max} - f_{\min}}\right),\ \mathbf{x} \in \Omega, \tag{1}$$

where $f_{\min} = \min_{\mathbf{x}\in\Omega} f(\mathbf{x})$ and $f_{\max} = \max_{\mathbf{x}\in\Omega} f(\mathbf{x})$ are the minimum and maximum values of $f(\mathbf{x})$ on the domain Ω, respectively. The parameter β controls the amplitude of the fingerprint image, implying that $-\beta \le f \le \beta$, and plays a critical role in the restoration. To restore the damaged regions of the fingerprint image, the data in the vicinity of the damaged area are used as boundary values. As the performance of the restoration is influenced by the value of β, it is important to select an appropriate value. Therefore, we define β based on the amplitude of the computational solution of the governing equation. A detailed discussion on this will be provided in Section 3.2.

The governing equation used for the restoration is the nonlocal CH equation [25], which is expressed as

$$\frac{\partial\phi(\mathbf{x},t)}{\partial t} = \Delta[F'(\phi(\mathbf{x},t)) - \epsilon^2\Delta\phi(\mathbf{x},t)] - \alpha(\phi(\mathbf{x},t) - \bar{\phi}),\ \mathbf{x} \in \Omega_{in},\ t > 0 \tag{2}$$

with the Dirichlet boundary condition as $\phi(\mathbf{x},\cdot) = \bar{f}(\mathbf{x}),\ \ \mathbf{x} \in \partial\Omega_{in}$ and $\bar{f}(\mathbf{x})$ is the scaled fingerprint image. Here, $\phi(\mathbf{x},t) \in [-1,1]$ represents the order parameter at spatial location $\mathbf{x}$ and time t, where $\phi = \pm 1$ indicates the pure phases, $F(\phi) = 0.25(\phi^2-1)^2$, ϵ and α are constants controlling the interface thickness and the nonlocal interaction, respectively, and $\bar{\phi}$ is the spatial average concentration of ϕ in Ω_{in}.

The nonlocal CH equation, which we adopt to restore damaged fingerprint images, is considered a phase-field model that simulates the microphase separation behavior of diblock copolymers. Diblock copolymers, composed of two covalently bonded polymer chains, self-assemble into periodic structures such as lamellae under appropriate thermodynamic conditions [27]. By modeling fingerprint ridges as analogous to these lamellar patterns, as shown in Fig. 2, the restoration process is formulated as the minimization of a nonlocal free energy functional.

The local interaction term promotes phase separation, while the nonlocal interaction term induces periodicity. Together, these effects lead to the formation of ridge-like structures within the damaged domain. When the domain has a curved boundary, the Dirichlet boundary condition is applied to obtain a lamellar pattern similar to fingerprint ridges, as shown in Fig. 3. Through this mechanism, the proposed model naturally reconstructs missing fingerprint textures without the need for external training data.

The discrete domain is defined as Ω^d, which consists of uniformly spaced grid points with grid size h. Fig. 1(b) shows the discretized

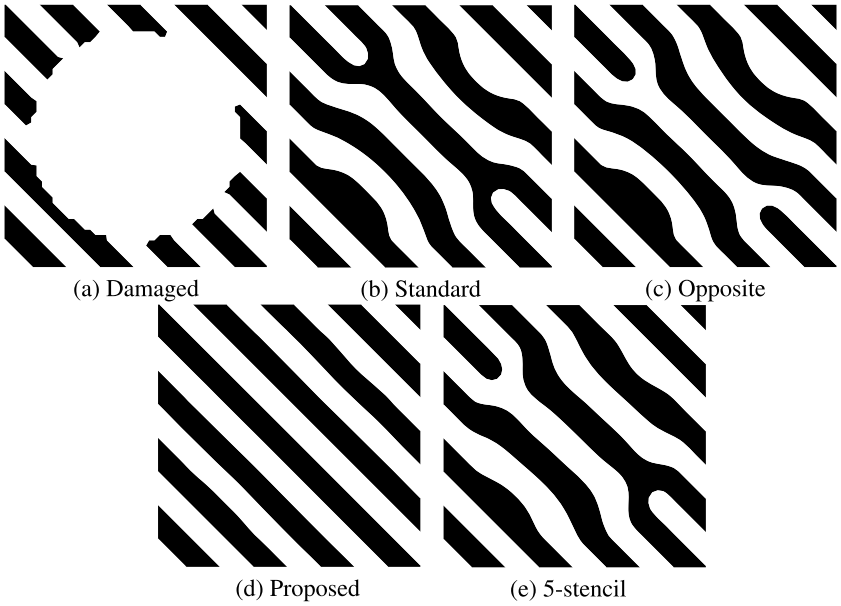

Fig. 6. Comparison of restoration results using different update orders: (a) Damaged input image, (b) Standard sweeping, (c) Opposite sweeping, (d) Spiral sweeping in proposed direction, and (e) 5-point stencil for the 2D Laplacian operator with proposed ordering.

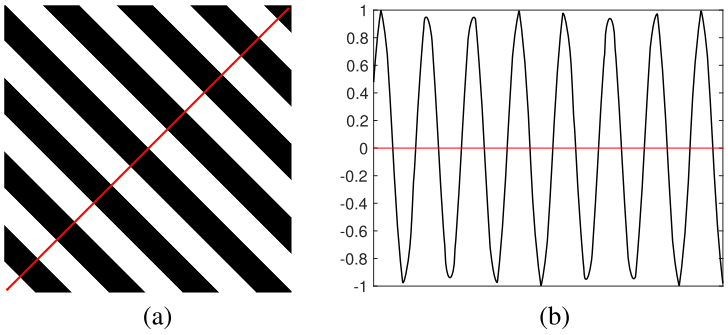

Fig. 7. Amplitude plots generated for the synthetic pattern images of $\hat{f}_1$.

domains: user-selected damaged discrete domain Ωin^d (open circles) with discrete boundary $\partial\Omega in^d$ (filled circles). Let $\Omega^d = \{(xi, y_j)|\ x_i = (i-0.5)h,\ y_j = (j-0.5)h,\ i = 1,\dots,N_x,\ j = 1,\dots,N_y\}$ be the set of center coordinates of the pixels whose union is a subset of the rectangular domain Ω, Ω^h_{in} (open circles) be the discrete domain and $\partial\Omega^h_{in}$ (filled circles) be the discrete boundary points, which consist of two layers outside Ω^h_{in} as displayed in Fig. 1 (b) with a pixel size h. Let $\bar{f}ij = \bar{f}(xi, yj)$ and $\phi^n_{ij} = \phi(x_i, y_j, n\Delta t)$, where Δt is the time step. Then, we use the following discrete equation for Eq. (2) [27]:

$$\frac{\phi^{n+1}_{i,j} - \phi^n_{i,j}}{\Delta t} = \Delta_h((\phi^n_{i,j})^3 - 3\phi^n_{i,j}) + 2\Delta_h\phi^{n+1}_{i,j} - \epsilon^2\Delta^2_h\phi^{n+1}_{i,j} - \alpha(\phi^{n+1}_{i,j} - \bar{\phi}), \quad (3)$$

where we use the 9-point isotropic stencil for the 2D Laplacian operator [28]:

$$\Delta_h\phi_{i,j} = \frac{1}{6h^2}\big[4(\phi_{i-1,j} + \phi_{i+1,j} + \phi_{i,j-1} + \phi_{i,j+1}) + \phi_{i-1,j+1} + \phi_{i+1,j+1} + \phi_{i+1,j-1} + \phi_{i-1,j-1} - 20\phi_{i,j}\big],$$

and $\Delta^2_h\phi_{i,j} = \Delta_h(\Delta_h\phi_{i,j})$. The isotropic Laplacian operator ensures accurate numerical solutions regardless of the orientation of the computational domain. Its rotational invariance eliminates dependency on directional alignment and is therefore particularly suitable for problems with radial or symmetric properties. By minimizing numerical anisotropy, it prevents artifacts caused by discretization bias. Additionally, its enhanced accuracy and stability contribute to reliable results, even in complex geometries. Due to these characteristics, we adopt the isotropic Laplacian operator to reduce directional bias in the computations. To efficiently solve Eq. (3), we apply a Saul'yev-type scheme [29]:

$$\begin{aligned}\frac{\phi^{n+1}_{i,j} - \phi^n_{i,j}}{\Delta t} &= \Delta_h((\phi^n_{i,j})^3 - 3\phi^n_{i,j}) + \frac{2}{6h^2}\big[4(\phi^*_{i-1,j} + \phi^*_{i+1,j} + \phi^*_{i,j-1} + \phi^*_{i,j+1}) \\ &\quad + \phi^*_{i-1,j+1} + \phi^*_{i+1,j+1} + \phi^*_{i+1,j-1} + \phi^*_{i-1,j-1} - 10\phi^{n+1}_{i,j} - 10\phi^n_{i,j}\big] \quad (4) \\ &\quad - \frac{\epsilon^2}{36h^4}\big[234\phi^{n+1}_{i,j} + 234\phi^n_{i,j} - 144(\phi^*_{i-1,j} + \phi^*_{i,j-1} + \phi^*_{i,j+1} + \phi^*_{i+1,j}) \\ &\quad - 8(\phi^*_{i-1j-1} + \phi^*_{i-1,j+1} + \phi^*_{i+1,j-1} + \phi^*_{i+1,j+1}) \\ &\quad + 18(\phi^*_{i-2,j} + \phi^*_{i,j-2} + \phi^*_{i,j+2} + \phi^*_{i+2,j}) \\ &\quad + 8(\phi^*_{i-2,j-1} + \phi^*_{i-2,j+1} + \phi^*_{i-1,j-2} + \phi^*_{i-1,j+2} \quad (5) \\ &\quad + \phi^*_{i+1,j-2} + \phi^*_{i+1,j+2} + \phi^*_{i+2,j-1} \\ &\quad + \phi^*_{i+2,j+1}) + (\phi^*_{i-2,j-2} + \phi^*_{i-2,j+2} + \phi^*_{i+2,j-2} + \phi^*_{i+2,j+2})\big] - \alpha(\phi^{n+1}_{i,j} - \bar{\phi}),\end{aligned}$$

where $\phi^*_{i,j} = \phi^{n+1}_{i,j}$ if $\phi^{n+1}_{i,j}$ is available and $\phi^*_{i,j} = \phi^n_{i,j}$ otherwise. Eq. (4) can be reformulated for updating the numerical solution as follows:

$$\begin{aligned}\phi^{n+1}_{i,j} &= \frac{1}{r}\Big[\frac{\phi^n_{i,j}}{\Delta t} + \Delta_h((\phi^n_{i,j})^3 - 3\phi^n_{i,j}) + \frac{2}{6h^2}\big[4(\phi^*_{i-1,j} + \phi^*_{i+1,j} + \phi^*_{i,j-1} + \phi^*_{i,j+1}) \\ &\quad + \phi^*_{i-1,j+1} + \phi^*_{i+1,j+1} + \phi^*_{i+1,j-1} + \phi^*_{i-1,j-1} - 10\phi^n_{i,j}\big] \quad (6) \\ &\quad - \frac{\epsilon^2}{36h^4}\big[234\phi^n_{i,j} - 144(\phi^*_{i-1,j} + \phi^*_{i,j-1} + \phi^*_{i,j+1} + \phi^*_{i+1,j}) \\ &\quad - 8(\phi^*_{i-1j-1} + \phi^*_{i-1,j+1} + \phi^*_{i+1,j-1} + \phi^*_{i+1,j+1}) + 18(\phi^*_{i-2,j} + \phi^*_{i,j-2} + \phi^*_{i,j+2} + \phi^*_{i+2,j}) \\ &\quad + 8(\phi^*_{i-2,j-1} + \phi^*_{i-2,j+1} + \phi^*_{i-1,j-2} + \phi^*_{i-1,j+2} + \phi^*_{i+1,j-2} + \phi^*_{i+1,j+2} + \phi^*_{i+2,j-1}\end{aligned}$$

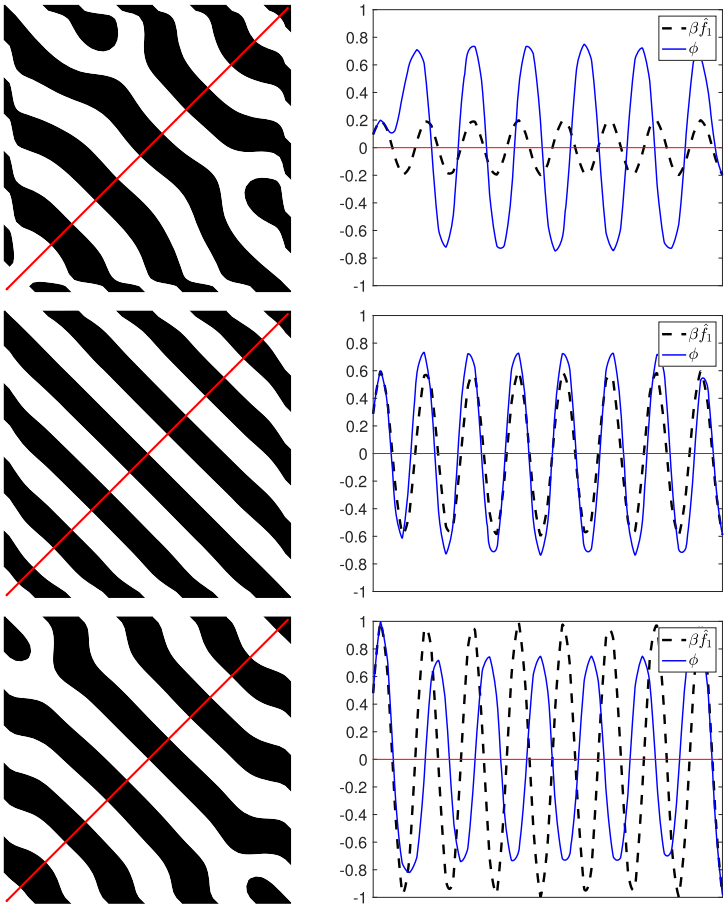

Fig. 8. Restoration results for damaged synthetic patterns under different β values, with $\beta = 0.2, 0.6$, and 1.0 shown from top to bottom. (a) Restored images, (b) Amplitude comparison of scaled data, $\beta\hat{f}_1$ (black), and numerical solutions, u (blue). (For interpretation of the references to colour in this figure legend, the reader is referred to the web version of this article.)

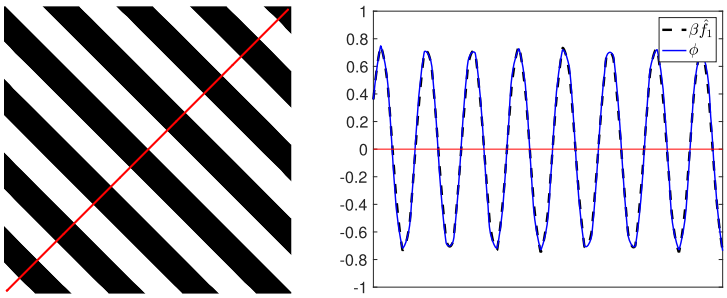

Fig. 9. Restoration results based on the determined value $\beta = 0.7512$ from the stable numerical solution.

$$+ \phi^*_{i+2,j+1}) + (\phi^*_{i-2,j-2} + \phi^*_{i-2,j+2} + \phi^*_{i+2,j-2} + \phi^*_{i+2,j+2})\big] + \alpha\bar{\phi}\Big],$$

where $r = 1/\Delta t + 10/3h^2 + 13\epsilon^2/2h^4 + \alpha$. We present an enhanced algorithm using a sweeping ordering approach, designed to compute numerical solutions with greater efficiency and reliability. Although the Gauss–Seidel iterative method is widely valued for its simplicity and effective convergence, it suffers from directional bias caused by its sequential update process. This bias stems from the fixed traversal pattern, often row or column-based, which can lead to uneven correction distribution across the domain. As a result, regions updated earlier can disproportionately impact the solution, potentially causing slower convergence or numerical inconsistencies, particularly in anisotropic or irregular domains. To overcome these limitations, techniques such as red-black ordering, multicolor strategies [30], and coupling with Jacobian methods [31] have been developed to reduce directional bias and improve convergence behavior.

In our proposed algorithm, for cases where damaged regions are partially embedded, the update process starts at an interior point adjacent to a boundary point and proceeds inward in a spiral pattern, systematically covering all grid points within Ω^d_{in}, as illustrated in Fig. 1(c). The proposed spiral sweeping ordering approach prioritizes updates near the boundary. It uses the accurate boundary values to sequentially update interior points. As a result, the solutions more accurately reflect the image's inherent information. In addition, to resolve directional bias, we alternate between clockwise (CW) and counterclockwise (CCW) updates in order to achieve a balanced and unbiased propagation of corrections across the domain. We note that the proposed algorithm inherently supports the handling of complex or multiply connected damaged regions,

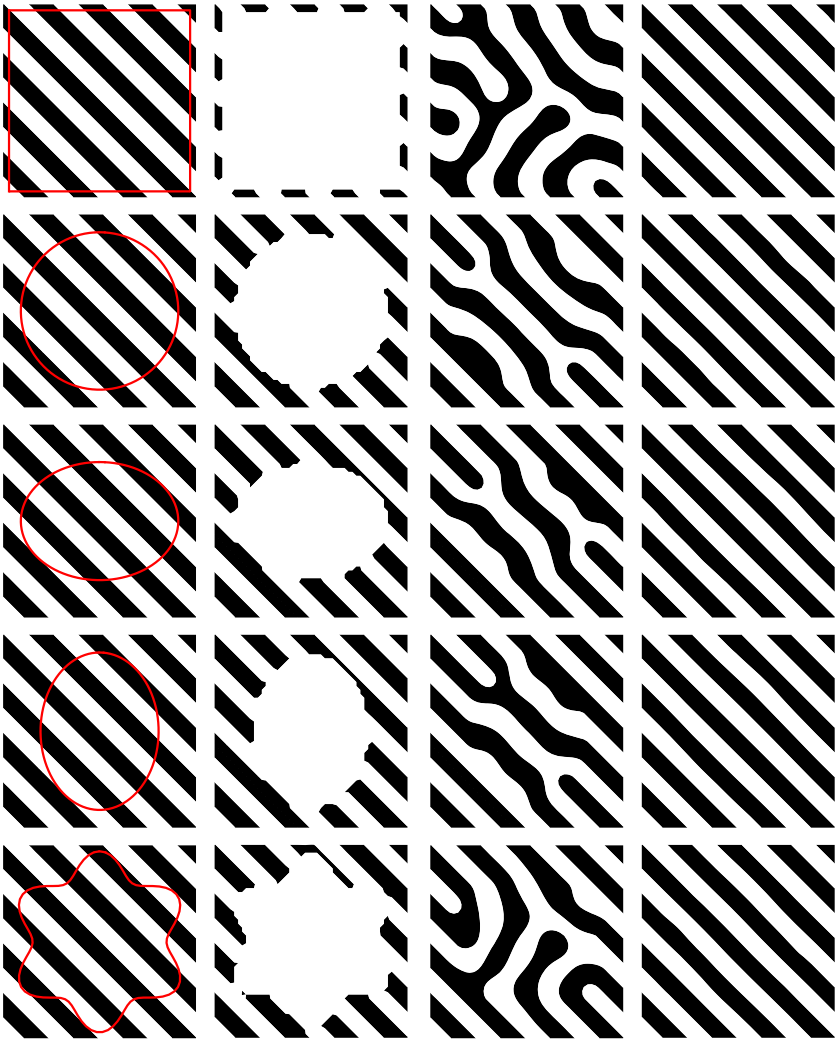

Fig. 10. Results of fingerprint restoration across different computational domains. (a) Intact images with the indicated computational domain (red lines), (b) damaged images, (c) and (d) restoration using the standard sweeping ordering and the proposed spiral sweeping ordering. (For interpretation of the references to colour in this figure legend, the reader is referred to the web version of this article.)

such as figure-eight-shaped domains. This is because the spiral sweeping update proceeds layer by layer from the boundary inward. This structure enables the method to naturally adapt to irregular geometries and multiple centers. As long as the boundary of the damaged region is properly defined, the algorithm systematically propagates corrections throughout the entire domain without requiring additional modification. This flexibility contributes to the generality and applicability of our approach to a broader class of damage configurations.

3. Numerical tests

We conduct computational analysis and simulation to evaluate the proposed spiral sweeping ordering method for fingerprint restoration. The initial and boundary conditions are given as

$$\phi_{ij}^0 = 0 \text{ on } \Omega_{in}^h \quad \text{and} \quad \phi_{ij}^n = \bar{f}_{ij} \text{ on } \partial\Omega_{in}^h,\ n = 0, 1, \dots, \tag{7}$$

respectively. The computational domain is restricted to the user-selected domain Ω_{in}^h. Unless specified otherwise, $h = 1$, $\Delta t = 0.2$, $\epsilon = 0.9$, and $\alpha = 0.09$ are used. Fig. 4 displays the time evolution of the damaged fingerprint image using the proposed spiral sweeping algorithm. From left to right, the iterations are $it = 0$, 100, 500, and 1000, respectively.

To quantitatively study the performance of the proposed method in restoring damaged fingerprints, we use the peak signal-to-noise ratio (PSNR) and the structural similarity index (SSIM):

$$\text{PSNR} = 10 \cdot \log_{10}\left(\frac{I_{\max}^2}{\text{mse}(I,P)}\right), \quad \text{mse}(I,P) = \frac{\sum_{i,j}\left(I_{i,j} - P_{i,j}\right)^2}{n_x n_y},$$

$$\text{SSIM} = \frac{(2\bar{I}\bar{P} + C_1)(2\sigma_{IP} + C_2)}{(\bar{I}^2\bar{P}^2 + C_1)(\sigma_I^2\sigma_P^2 + C_2)}$$

where $I_{i,j} = f_{i,j}/(f_{\max} - f_{\min})$, n_x and n_y are the number of pixels in the x- and y-directions, respectively, $P_{i,j} = 0.5(\phi_{i,j} + 1)$, $\bar{I}$ and $\bar{P}$ denote the means of I and P, respectively, and σ_I^2, σ_P^2 represent their variances. In addition, $\text{Cov}(I,P)$ is the covariance of I and P, and $C_1 = 0.0001$, $C_2 = 0.0009$. Higher PSNR and SSIM values show better restoration quality for the fingerprint image.

We proceed to evaluate and compare the performance of the standard ordering algorithm and the proposed spiral ordering algorithm on both synthetic and real images. The first synthetic pattern $\hat{f}_1$ consists of diagonal lines, while the second pattern $\hat{f}_2$ features curved lines, see Fig. 5. These patterns are as follows:

$$\hat{f}_1(x,y) = \sin(0.5(x+y)),\ \hat{f}_2(x,y) = \sin(0.7\sqrt{x^2+y^2}),\quad \text{on } \Omega = [0,50]\times[0,50],$$

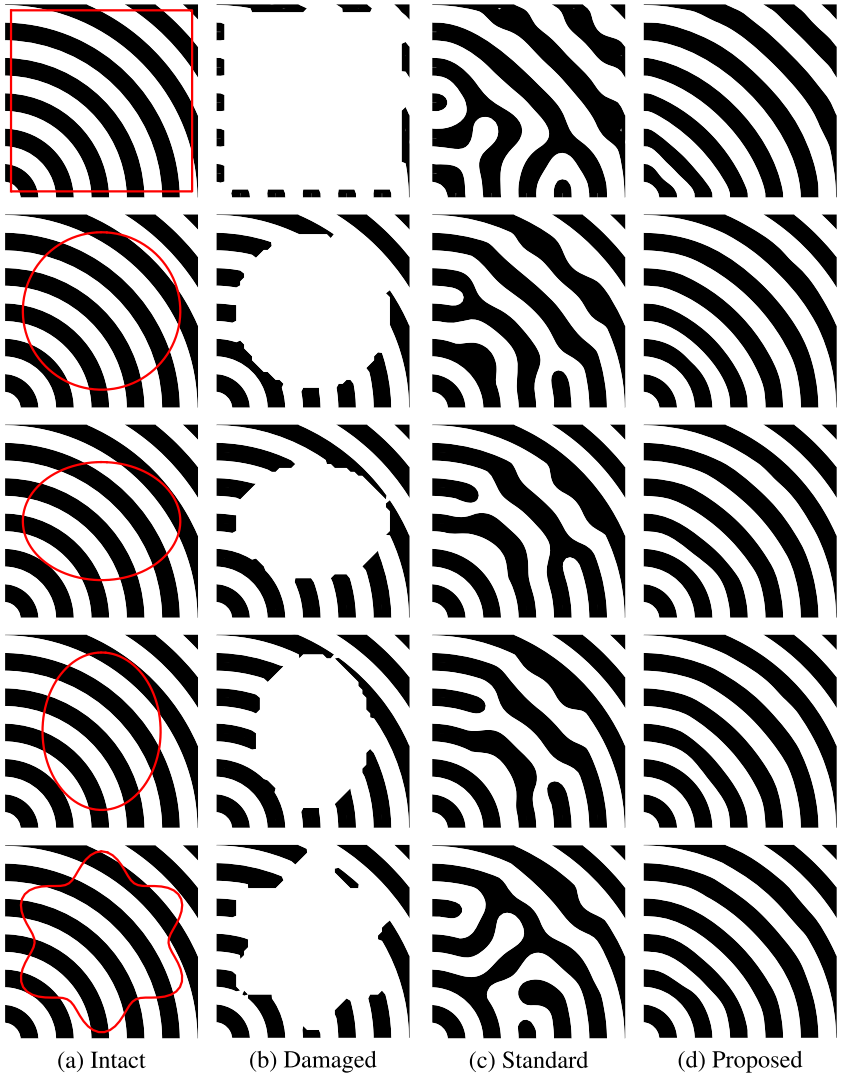

Fig. 11. Results of fingerprint restoration with different computational domains. (a) Intact image with the indicated computational domain(red line), (b) damaged image, (c) and (d) restoration using the standard sweeping ordering and the proposed spiral sweeping ordering. (For interpretation of the references to colour in this figure legend, the reader is referred to the web version of this article.)

3.1. Effect of the sweeping ordering and the isotropic Laplacian stencil

In Gauss–Seidel-type iterative methods, the order in which grid points are updated may cause directional bias. This occurs because each updated value is immediately used in the next update, which causes information to flow more strongly along the sweeping direction. As a result, the numerical solution may exhibit direction-dependent errors. To observe the effect of the isotropic Laplacian operator, we also compare the results obtained using a standard 5-point stencil for the Laplacian. To examine the influence of sweeping direction and the 5-point stencil for the Laplacian operator on the results, we compared three different update strategies for solving the numerical problem:

1. **Standard order**: The outer loop increments the index i, and the sweep proceeds in the x-direction from left to right. The inner loop increments the index j and updates the values in the y-direction from bottom to top. The update sequence proceeds as follows:

$$(i, j) = (1, 1) \to (1, 2) \to \cdots \to (1, N_y) \to (2, 1) \to \cdots \to (N_x, N_y)$$

That is, the computation starts at the bottom-left corner of the domain and proceeds upward along each column. It then moves from the leftmost column to the rightmost one in sequence.

2. **Opposite order**: This sweeping order performs the computation in the opposite direction to the standard order. The outer loop decreases the index i, and the sweep proceeds in the x-direction from right to left. The inner loop decreases the index j and updates the values in the y-direction from top to bottom. The update sequence proceeds as follows:

$$(i, j) = (N_x, N_y) \to (N_x, N_y - 1) \to \cdots \to (N_x, 1) \to (N_x - 1, N_y) \to \cdots \to (1, 1)$$

That is, the computation starts at the top-right corner of the domain and proceeds downward along each column. It then moves from the rightmost column to the leftmost one in sequence.
3. **Proposed order**: The update alternates between counterclockwise and clockwise directions at each iteration. This alternating scheme helps reduce directional influence that accumulates during iteration.
4. **5-stencil Laplacian**: The 5-point stencil for the 2D Laplacian operator with the proposed ordering

$$\Delta_h \phi_{i,j} = (\phi_{i-1,j} + \phi_{i+1,j} + \phi_{i,j-1} + \phi_{i,j+1} - 4\phi_{i,j})/h^2,$$

For this test, we used the synthetic example $\hat{f}_1$ with a circular damaged region of radius $r = 20$, shown in Fig. 6(a).

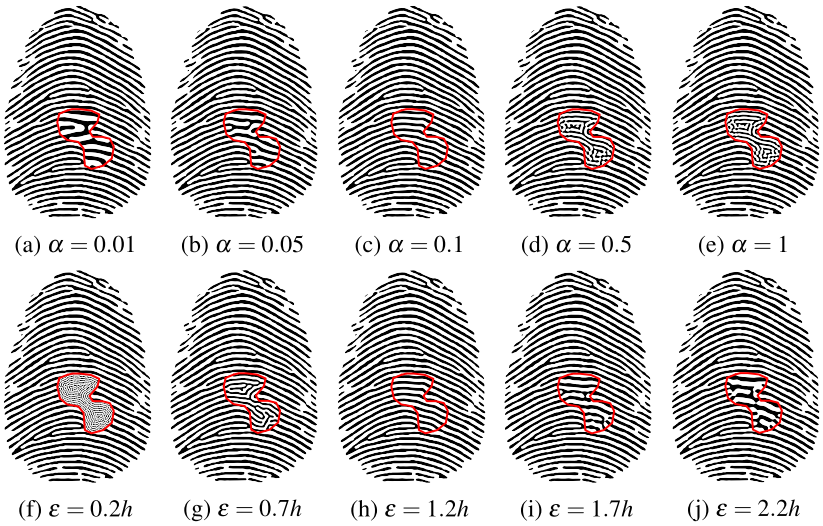

Fig. 12. Sensitivity analysis with respect to the parameters α and ϵ. The top row (a)–(e) shows the restoration results with varying $\alpha = 0.01$, 0.05, 0.1, 0.5, and 1.0, respectively, while fixing $\epsilon = 1.2h$. The bottom row (f)–(j) displays the computational results with varying $\epsilon = 0.2h$, $0.7h$, $1.2h$, $1.7h$, and $2.2h$, respectively, while fixing $\alpha = 0.1$. The red contour indicates the damaged region. The results demonstrate the effect of parameter selection on restoration quality and pattern continuity. Modified from [25], with permission from Elsevier. (For interpretation of the references to colour in this figure legend, the reader is referred to the web version of this article.)

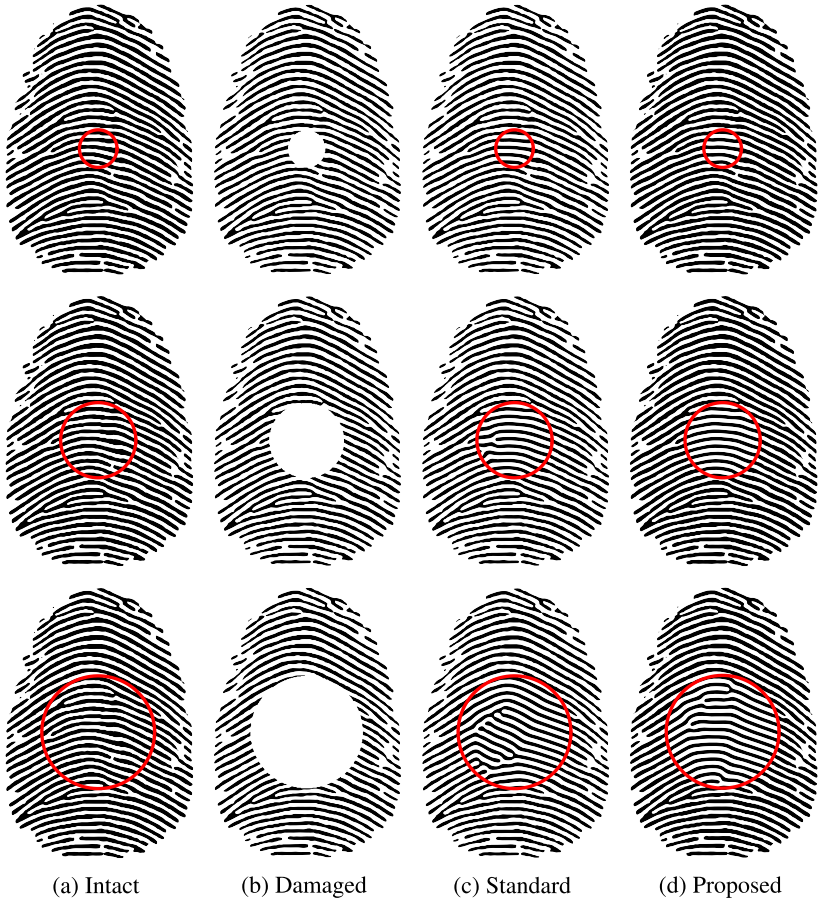

Fig. 13. Restoration results of fingerprint images with varying sizes of the circular damaged regions. (a) Intact images, (b) damaged images, (c) restoration results using the standard algorithm, and (d) restoration results using the proposed algorithm. From top to bottom, the sizes of the damaged regions are $r = 30, 60$, and 90. Modified from [25], with permission from Elsevier.

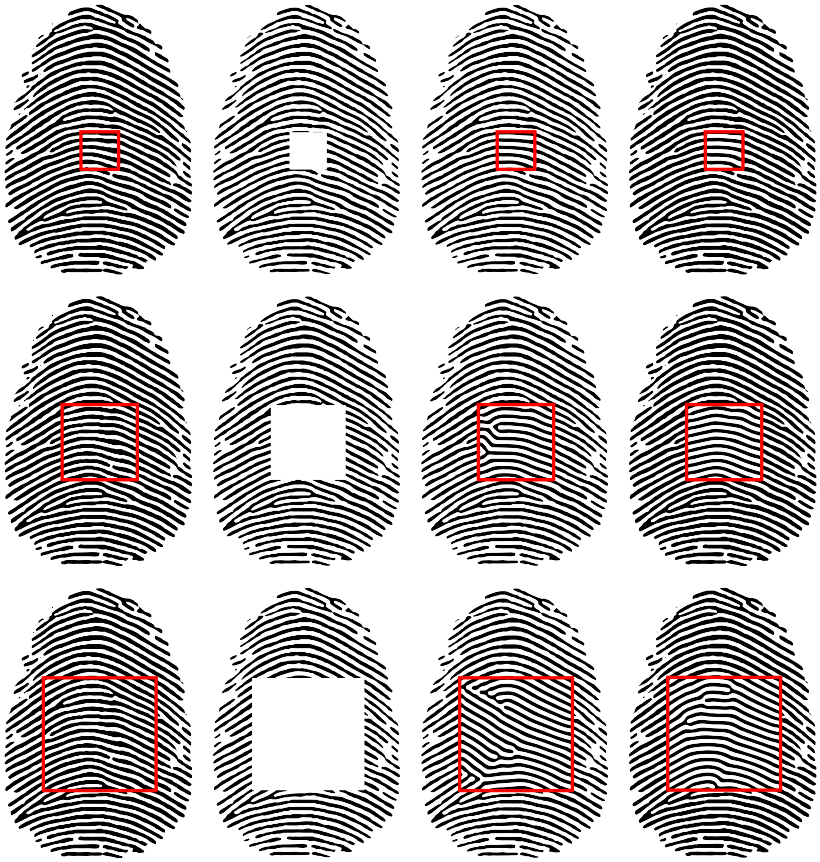

Fig. 14. Restoration results of fingerprint images with varying sizes of the square damaged regions. (a) Intact images, (b) damaged images, (c) restoration results using the standard algorithm, and (d) restoration results using the proposed algorithm. From top to bottom, the sizes of the damaged regions are $r = 30, 60$, and 90. Modified from [25], with permission from Elsevier.

Table 1
Performance comparison of PSNR and SSIM for the three different update strategies and the 5-stencil Laplacian.

	Standard	Opposite	Proposed	5-stencil
PSNR	8.9177	8.9092	35.4944	11.1870
SSIM	0.4360	0.4352	0.9974	0.5202

Fig. 6(b)–(d) shows the restoration results for three update strategies: Standard sweeping, opposite sweeping, and the proposed spiral method. The standard and opposite results reveal directional bias. In the standard case, distortions appear in the bottom-right region, while in the opposite case, similar artifacts occur in the top-left region. These distortions result from the one-sided propagation of information caused by the fixed update order. The proposed method reconstructs the diagonal patterns with consistent spacing and orientation. The result is close to the ground truth, and bias from the update direction does not appear. Fig. 6(e) shows that the diagonal pattern is blurred due to the low isotropy of the 5-point stencil. Table 1 provides quantitative evidence for these observations by reporting the PSNR and SSIM values obtained using three update strategies and the 5-point stencil Laplacian. The proposed algorithm demonstrates superior performance compared to the other update strategies and the 5-point stencil Laplacian, and it results in the highest reconstruction accuracy.

3.2. Effect of the scaling factor β

The parameter β determines the amplitude range of the fingerprint image and significantly impacts the restoration process. To restore the damaged regions in the fingerprint image, boundary values are set from the surrounding intact data near the damaged area. Since the restoration performance is highly sensitive to the choice of β, selecting an optimal value is essential. Fig. 7 presents the amplitude distribution of the synthetic image for $\beta = 1$. In particular, the red line in Fig. 7 (a) indicates the axis along which the amplitude values are analyzed, and it provides a reference for evaluating the behavior of the numerical solution.

As demonstrated in Fig. 8, the performance of the proposed algorithm is evaluated for different values of the parameter β. Specifically, the values of β considered are $0.2, 0.6$, and 1.0, with the corresponding amplitude distributions depicted in Fig. 8 (b). In Fig. 8 (b), the black dashed line represents the amplitude of the image data scaled by β, while the blue solid line is the amplitude of the numerical solution derived from the governing equation. Near the domain boundaries, the two graphs exhibit strong agreement, indicating consistency; however, as the evaluation progresses toward the center of the domain, a significant divergence between the numerical solution and the actual data becomes evident. This discrepancy suggests that the restoration of the damaged region is not fully achieved. The restoration outcomes for the three tested values of β are presented in Fig. 8 (a). Among them, the case of $\beta = 0.6$ produced the most favorable outcome, with the amplitude and wavelength of the restored solution closely matching those of the original data. Table 2 provides quantitative evidence for these observations by reporting the PSNR and SSIM values obtained for $\beta = 0.2, 0.6$ and 1.0.

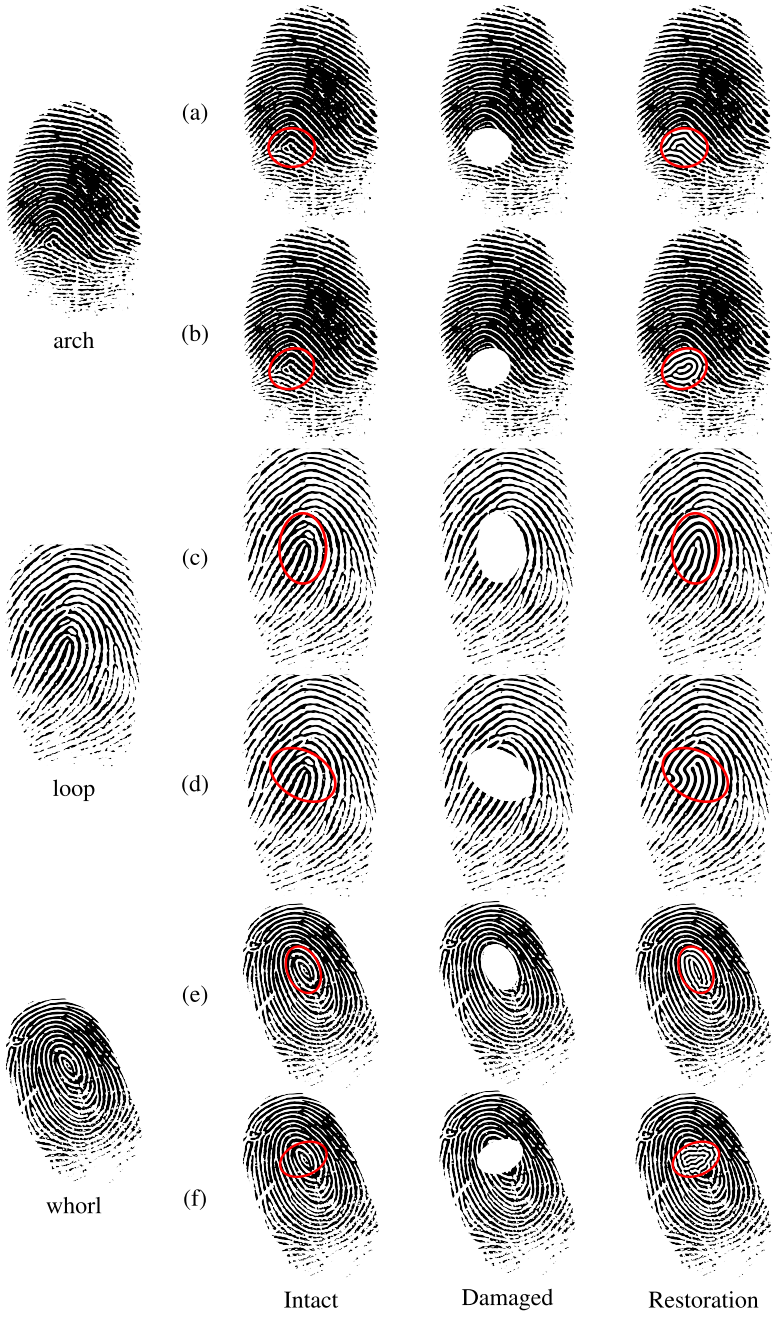

Fig. 15. The diverse fingerprint patterns. The first column images are the original images from the FVC 2004 dataset. (a), (c), (e) Proper restoration results. (b), (d), (f) Improper restoration results.

Table 2
PSNR and SSIM values for damaged synthetic patterns under $\beta = 0.2$, 0.6, and 1.0.

β	0.2	0.6	1.0
PSNR	12.5763	20.8480	6.8171
SSIM	0.2763	0.9248	0.0691

Furthermore, this suggests that $\beta = 0.6$ provides a good balance between numerical stability and solution accuracy for the proposed algorithm. However, further refinement of the β value is necessary to confirm its optimality.

Thus, β is defined in relation to the amplitude of the numerical solution for the governing equation, Eq. (3). To determine β, we first obtain a stable numerical solution for $\beta = 1$ and then select a β value that matches the amplitude of the numerical solution to that of the governing equation before proceeding with the fingerprint restoration process. Fig. 9 shows the results adjusted to correspond to the amplitude of the numerical solution, with the determined value $\beta = 0.7512$. The corresponding PSNR and SSIM values are 34.9252 and 0.9968, respectively.

3.3. Comparison based on the geometry of the damage area

We compare the performance of the standard row or column-based ordering with the proposed spiral sweeping ordering algorithm for fin-

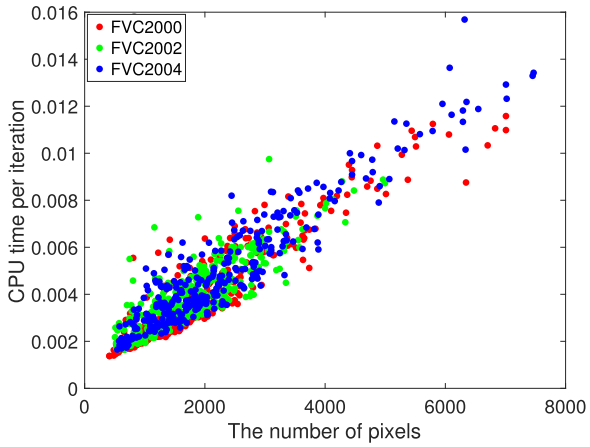

Fig. 16. CPU time per iteration with respect to the number of pixels for the FVC2000, FVC2002, and FVC2004 datasets. The results show a linear relationship that reflects the proportional increase in computational cost with respect to image size.

gerprint image restoration. We performed experiments on various geometric computational domain shapes for the synthetic image $\hat{f}$, including square, circular, elliptical, and polar rose domains. The equations defining each computational domain are as follows:

$$\begin{aligned}
\Omega_{in}^{square} &= \{(x,y)|\ 2 \le x \le 48,\ 2 \le y \le 48\},\\
\Omega_{in}^{circle} &= \{(x,y)|\ \sqrt{(x-25)^2+(y-25)^2} \le 20\},\\
\Omega_{in}^{ellipse_r} &= \{(x,y)|\ \frac{(x-25)^2}{20^2}+\frac{(y-25)^2}{15^2} \le 1\},\\
\Omega_{in}^{ellipse_c} &= \{(x,y)|\ \frac{(x-25)^2}{15^2}+\frac{(y-25)^2}{20^2} \le 1\},\\
\Omega_{in}^{rose} &= \{(x,y)|\ \sqrt{(x-25)^2+(y-25)^2} \le r(\theta),\\
&\quad r(\theta) = 20 + 3(32\cos^6(\theta) - 48\cos^4(\theta) + 18\cos^2(\theta) - 1)\},\ \theta \in [0, 2\pi].
\end{aligned}$$

Fig. 10 (a) illustrates the computational domains delineated by red solid lines, with the patterns inside these domains representing the ground truth. To assess restoration performance, the domains are artificially damaged by initializing their data values to zero, as shown in Fig. 10 (b). Restoration is subsequently performed using each of the two methods: the conventional ordering method and the proposed spiral ordering approach. Fig. 10 (c) and (d) display the restoration outcomes obtained using the standard ordering and spiral ordering methods, respectively. As evident from the results, the standard ordering method fails to accurately reconstruct the patterns within all geometric domains, whereas the proposed spiral ordering method successfully recovers the original patterns. These results substantiate the robustness of the proposed ordering strategy in producing reliable numerical solutions, irrespective of geometric variations in the computational domain. Fig. 11 presents the identical test results for the synthetic image $\hat{f}_2$, and it is evident that the restoration results effectively capture the curved patterns as well.

3.4. Parameter sensitivity analysis

We conduct a parameter sensitivity analysis for the nonlocal parameter α and the regularization parameter ϵ in the proposed method. The parameter α controls the attraction toward the spatial average $\bar{\phi}$, and ϵ determines the strength of the fourth-order diffusion term $\epsilon^2\Delta_h^2\phi$, which affects the smoothness and thickness of the transition region. Fig. 12 shows restoration results for different values of these parameters. For the effect of α, the parameter ϵ was fixed at $1.2h$, and α was set to 0.01, 0.05, 0.1, 0.5, and 1.0, as shown in Fig. 12(a)–(e). When $\alpha = 0.01$, the global average term had little effect. The restored region contained irregular structures that did not align with the surrounding pattern. When $\alpha = 0.1$, the restored pattern matched the original structure in direction and wavelength. When $\alpha = 1.0$, the global force dominated, and the result became over-smoothed; as a result, the ridges collapsed or vanished. These results show that α is inversely related to the spatial wavelength and must be selected carefully. For the effect of ϵ, the parameter α was fixed at 0.1, and ϵ was tested at $0.2h$, $0.7h$, $1.2h$, $1.7h$ and $2.2h$ as shown in Fig. 12(f)–(j). When $\epsilon = 0.2h$, the regularization effect was weak, and noisy artifacts appeared inside the damaged area. When $\epsilon = 2.2h$, excessive smoothing caused the loss of fine ridge structures. The best result was observed at $\epsilon = 1.2h$, where the restored pattern preserved both clarity and structural consistency. These results confirm that the model behavior depends strongly on both α and ϵ, and each must be chosen based on the desired restoration quality.

3.5. Effect of damaged domain size

We present simulations conducted for various damage sizes. The selected parameters are $\epsilon = 1.2$ and $\alpha = 0.1$. The damaged regions are

$$\begin{aligned}
\Omega_{in}^{square} &= \{(x,y)|\ |x-170| \le 2r, |y-250| \le 2r\},\\
\Omega_{in}^{circle} &= \{(x,y)|\ \sqrt{(x-165)^2+(y-210)^2} \le r\}
\end{aligned}$$

with $r = 30,\ 60$, and 90, respectively.

Figs. 13(c)–(d) and 14(c)–(d) illustrate the restoration results of damaged fingerprint images for varying shapes and sizes of the damaged regions, using the standard ordering method and the proposed spiral ordering method. By visually comparing the reference images used as the ground truth in Figs. 13(a) and 14 (a) with the restoration results, it is evident that the proposed algorithm achieves superior restoration quality compared to the standard method. The proposed method demonstrates its ability to more accurately reconstruct the damaged regions and preserves finer details and the overall structure, which results in superior performance compared to the standard approach. As shown in both figures, the standard method's performance deteriorates significantly when the damage size increases beyond $r = 60$. The reconstructed patterns lose coherence, and discrepancies with the ground truth become apparent. In contrast, the proposed spiral sweeping ordering method maintains high restoration quality even for larger damage sizes, with only minor degradation observed for $r = 90$.

Table 3 quantitatively supports these findings by presenting the PSNR and SSIM values for different damaged region sizes ($r = 30,\ 60,\ 90$) and shapes (circle and square). For both images, the proposed method consistently outperforms the standard method. For example, in circular regions with $r = 90$, the proposed method achieves a PSNR of 16.0902 and an SSIM of 0.8745, compared to the standard method's PSNR of 12.9883 and SSIM of 0.6951. These computational results highlight the robustness of the proposed algorithm in accurately restoring fingerprint patterns even in the presence of large damaged areas. The improved performance of the proposed method can be attributed to its spiral sweeping approach, which effectively uses boundary information to update interior points in a balanced manner. By alternating between clockwise and counterclockwise updates, the algorithm minimizes directional bias and ensures that the restoration process remains stable and accurate across various damage sizes and geometries. These computational results confirm the effectiveness and reliability of the proposed algorithm for restoring damaged fingerprint images.

3.6. Restoration of diverse fingerprint patterns

To further validate the robustness and generalizability of the proposed restoration method, we conduct experiments on a diverse set of fingerprint patterns, including whorls, loops, and arches, using the FVC 2004 dataset. Fig. 15 illustrates representative examples of the restoration results across these fingerprint types. In Fig. 15, the damaged regions are

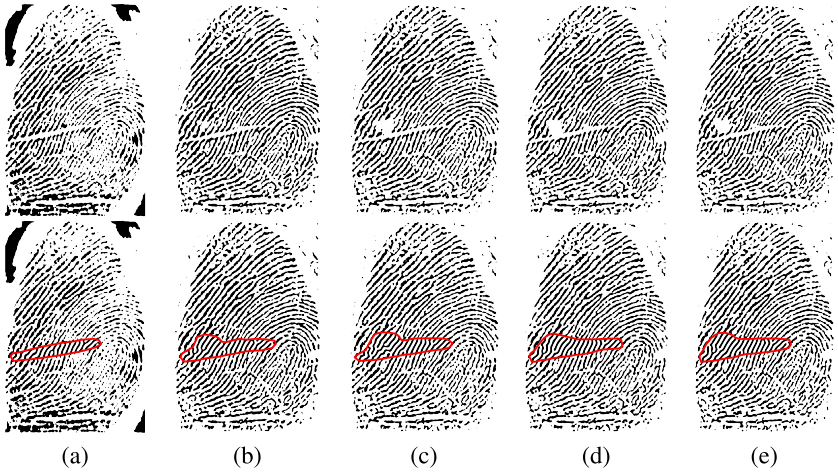

Fig. 17. Future work direction combining the deep learning technique with the proposed method for improved fingerprint restoration. These results were obtained by applying our method to the outputs generated by the GAN-based approaches: (a) Original input image, (b) MC-GAN [13], (c) MU-GAN [35], (d) Cycle-GAN [36], and (e) DU-GAN [37]. Modified from [13], with permission from Springer.

Table 3
Performance comparison of PSNR and SSIM for different damaged region sizes ($r = 30, 60, 90$).

Method	Standard			Proposed		
Circle: r	30	60	90	30	60	90
PSNR	17.2941	16.2542	12.9883	31.3145	23.5726	16.0902
SSIM	0.7461	0.7418	0.6951	0.9910	0.9574	0.8745
Square: r	30	60	90	30	60	90
PSNR	16.7110	16.0696	11.7431	29.0283	21.3015	14.7552
SSIM	0.7296	0.7416	0.6626	0.9358	0.9574	0.8430

Table 4
Parameters for arch, loop, and whorl fingerprint restoration tests.

	h	Δt	ϵ	α
arch	1.0	$0.2h^2$	h	0.15
loop	1.0	$0.2h^2$	$1.05h$	0.14
whorl	1.0	$0.2h^2$	$1.15h$	0.60

$$\Omega_{in}^{arch} = \left\{ (x,y) \middle| \frac{(x-100)^2}{42^2} + \frac{(y-140)^2}{35^2} \le 1 \right\}, \tag{8}$$

$$\Omega_{in}^{loop} = \left\{ (x,y) \middle| \frac{(x-100)^2}{35^2} + \frac{(y-190)^2}{42^2} \le 1 \right\}, \tag{9}$$

$$\Omega_{in}^{whorl} = \left\{ (x,y) \middle| \frac{(x\cos(\frac{\pi}{8}) - y\sin(\frac{\pi}{8}) - 130)^2}{35^2} + \frac{(x\sin(\frac{\pi}{8}) + y\cos(\frac{\pi}{8}) - 240)^2}{52.5^2} \le 1 \right\}. \tag{10}$$

In Fig. 15, the first column shows the original fingerprints of three types, which are arch, loop, and whorl. The second column shows intact fingerprints images with the region to be damaged. The third column shows damaged fingerprint images, and the fourth column shows restoration results. Fig. 15(a), (c), and (e) illustrate proper restoration, whereas Fig. 15(b), (d), and (f) illustrate improper restoration. Because the distinction between proper and improper restoration is visually evident, the comparison is made in a qualitative manner against the original fingerprint data. The damaged regions in (a), (c), and (e) are given by Eqs. (8)–(10), respectively. The regions in (b), (d), and (f) are obtained by rotating the regions defined in Eqs. (8)–(10) about the center of the ellipse by $-\pi/3$, $\pi/3$, and $-\pi/2$, respectively. Table 3.6 presents the parameter values used in the restoration tests for arch loop and whorl fingerprints.

The experimental results show that the proposed method can successfully recover ridge continuity and orientation in most cases, as shown in Fig. 15(a), (c), and (e). However, the restoration performance is sensitive to the definition of damaged regions, and areas containing singular points such as cores and deltas remain vulnerable, as highlighted in Fig. 15(b), (d), and (f). These limitations arise because, depending on the definition of the damaged regions, fingerprints with singular points may not provide sufficient surrounding data for accurate inference. Consequently, even with the use of ordering algorithms, the restoration exhibited inherent limitations in these cases. These findings show that further refinement is necessary to improve robustness when damage occurs in complex topological regions.

3.7. Comparison test

To compare the effectiveness of our approach with existing techniques, we calculated the PSNR and contrasted it with the outcomes reported by other state-of-the-art fingerprint restoration methods [11,25]. Table 5 presents the average PSNR values obtained by our method and various existing models on corrupted fingerprint images derived from the FVC 2004 dataset [32]. Based on the computational results in Table 5, our algorithm demonstrates better performance than the Gabor filtering, BaseNet, BaseNet-bin, and the method proposed by Li et al. Although the PSNR from our method is marginally below that of the OFFIENet-tri-shared model [11], it is important to note that the comparison lacks complete fairness. This is because our method does not require extensive training on large-scale fingerprint datasets and achieves competitive results by using only a small portion of the fingerprint specifically, local information near the corrupted regions instead of using the entire image. In contrast, deep learning-based approaches require substantial training costs to reach similar levels of accuracy. In addition, due to the unavailability of implementations for existing methods, a direct SSIM-based comparison could not be conducted. Nevertheless, the proposed algorithm attained a high SSIM score of 0.9863, which suggests that the restored images preserve structural similarity to the ground truth to a high degree.

Finally, to evaluate the computational performance of the proposed algorithm, we measured the average restoration time and the average CPU time per iteration. The evaluation was conducted on the FVC2000, FVC2002, and FVC2004 datasets. All computations were carried out in a MATLAB R2024a environment on a computer with a 12th Gen Intel(R) Core(TM) i9-12900K 3.20 GHz CPU and 32 GB of RAM. Table 6 shows the average restoration time of the proposed al-

Table 5
Comparison of the average PSNR values under the SN + Sc corruption condition on the FVC2004 dataset between the proposed method and other fingerprint restoration models.

Method	SN + Sc(FVC2004)
No enhancement	8.07
Gabor filtering	7.12
BaseNet	18.93
BaseNet-bin	19.61
BaseNet-tri	**21.67**
BaseNet-tri-shared	21.28
Li et al.	19.89
Our method	21.19

Table 6
Average restoration time (in seconds) using the proposed method on the FVC2000, FVC2002, and FVC2004 datasets.

Datasets	DB1_B	DB2_B	DB3_B	DB4_B
FVC2000 [33]	4.1128	2.9627	9.2276	3.0499
FVC2002 [34]	6.6402	5.1489	3.7792	3.7703
FVC2004 [32]	10.7250	4.5904	5.1112	3.8390

gorithm for each dataset. Fig. 16 displays the CPU time per iteration with respect to the size of the computational domain. The computational cost of the proposed method, which follows the Gauss–Seidel algorithm, increases linearly with image size. In addition, the results in Table 6 demonstrate that the computational cost is not expensive, which implies that the proposed algorithm has high computational efficiency.

Deep learning methods such as CNNs and GANs show strong performance in image restoration. However, they require high-quality labeled data for training. The proposed PDE-based method does not depend on training data and uses only local information near the damaged region, defined by boundary data in the computational domain. The restoration accuracy is lower than that of deep learning models, but this method introduces a different direction for solving fingerprint restoration problems. We plan to combine this method with CNN or GAN architectures in future work. For example, the first row of Fig. 17 shows degraded fingerprint images along with the restoration results produced by a GAN-based method. In these results, several regions remain unrecovered, which reveals the limitations of the method in handling severe distortions. When our algorithm is applied to those missing or poorly restored areas, the reconstructed output shows noticeable improvement, as presented in the second row of Fig. 17. This finding supports the possibility that combining our approach with machine learning or deep learning methods could lead to more complete and accurate fingerprint restoration results in future applications.

4. Conclusions

In this study, we proposed a novel sweeping ordering algorithm to reconstruct partially damaged fingerprint images using the nonlocal CH equation. The algorithm leverages an efficient spiral sweeping ordering approach combined with the Gauss–Seidel-type update method and the isotropic Laplacian operator. The use of Dirichlet boundary conditions and the careful scaling of the amplitude parameter β ensured that the numerical solution closely matched the inherent properties of the damaged fingerprint image. The isotropic Laplacian operator was particularly effective in maintaining rotational invariance and minimizing numerical anisotropy, leading to robust and accurate solutions independent of the computational domain's geometry. Numerical experiments demonstrated that the proposed spiral sweeping ordering method significantly outperforms the standard row or column-based ordering in restoring damaged patterns. By alternating between clockwise and counterclockwise updates, the algorithm effectively reduced directional bias, enabling consistent performance across various geometric domains, including square, circular, elliptical, and rose-shaped regions. Overall, the proposed method provides a reliable and efficient framework for fingerprint restoration, offering robustness against variations in domain shape and damage size. In addition, we plan to integrate the proposed method with CNN or GAN models to achieve improved results in fingerprint restoration. Restoring missing ridges in latent fingerprints through manual reconstruction is a labor-intensive, time-consuming, and costly procedure. Latent fingerprint ridges are often degraded due to smudging, partial loss, or aging effects. Such fingerprints cannot be directly used in a court of law to obtain a conviction unless they are matched to known fingerprints. However, the application of the proposed fingerprint restoration methods to the reconstruction of these prints can effectively reduce the number of potential suspects and contribute to the identification of individuals who have gone missing, thereby resulting in a significant reduction in human resource costs. Furthermore, as future work, the consideration of methods such as the Multi-Scale Attention Pyramid Vision Transformer (MSAPTV) [38] and genetic algorithms [39] for the automatic selection of damaged fingerprint regions can be proposed in order to improve the proposed PDE-based scheme into an automated reconstruction method that minimizes manual restoration. As a result, these future works could minimize manual restoration and contribute to systems such as the automatic fingerprint identification system (AFIS) [40].

CRediT authorship contribution statement

Sangkwon Kim: Writing – review & editing, Writing – original draft, Visualization, Software, Methodology, Investigation; **Yibao Li:** Writing – review & editing, Validation, Methodology, Investigation; **Soobin Kwak:** Writing – original draft, Visualization, Methodology, Investigation; **Junseok Kim:** Writing – review & editing, Validation, Supervision, Methodology.

Data availability

Data will be made available on request.

Declaration of competing interest

The authors declare that they have no known competing financial interests or personal relationships that could have appeared to influence the work reported in this paper.

Acknowledgement

The first author (S.K. Kim) was supported by the National Research Foundation of Korea (NRF) grant funded by the Korea government(MSIT) (No. 2022R1C1C2005275). The corresponding author (J.S Kim) was supported by Korea University Grant (No. K2504591). We sincerely thank the reviewers for their constructive feedback and insightful comments.

References

[1] A.A.A. Hamid, M.S.M. Rahim, A.S. Al-Mazyad, T. Saba, Analysis of proposed noise detection & removal technique in degraded fingerprint images, D Res .3 (2015) 38.
[2] D.K. Misra, S.P. Tripathi, A study report on fingerprint image enhancement methods, IJCSC International Journal of Computer Science & Communications (IJCSC), 3 (2012) 163–170.
[3] X. Yang, D. Wang, Z. Yang, A fingerprint inpainting technique using improved partial differential equation methods, in: Proc. Int. Conf. Graph. Image Process, Int. Conf. Graph. Image ess, 2011, p. 828571.
[4] I. Joshi, T. Prakash, B.S. Jaiswal, R. Kumar, A. Dantcheva, S.D. Roy, P.K. Kalra, Context-aware restoration of noisy fingerprints, IEEE Sens. Lett. 6 (10) (2022) 1–4.

[5] J. Khodadoust, M.A. Medina-Pérez, O. Loyola-González, R. Monroy, A.M. Khodadoust, A secure and robust indexing algorithm for distorted fingerprints and latent palmprints, Expert Syst. Appl. 206 (15) (2022) 117806.
[6] S.A. Bouhamed, I.K. Kallel, E. Bossé, B. Solaiman, Two no-reference image quality assessment methods based on possibilistic Choquet integral and entropy: application to automatic fingerprint identification systems, Expert Syst. Appl. 224 (15) (2023) 119926.
[7] S. Saponara, A. Elhanashi, Q. Zheng, Recreating fingerprint images by convolutional neural network autoencoder architecture, IEEE Access 9 (2021) 147888–147899.
[8] T.S. Sasikala, A secure multi-modal biometrics using deep ConvGRU neural networks based hashing, Expert Syst. Appl. 235 (2024) 121096.
[9] H. Gao, Y. Zhang, J. Yang, D. Dang, Mixed hierarchy network for image restoration, Pattern Recognit. 161 (2025) 111313.
[10] S. Shreya, K. Chatterjee, Latent fingerprint and iris fusion for enhancement of performance of human identification system, Expert Syst. Appl. 235 (2024) 121208.
[11] W.J. Wong, S.H. Lai, Multi-task CNN for restoring corrupted fingerprint images, Pattern Recognit. 101 (2020) 107203.
[12] N.S. Cho, C.S. Kim, C. Park, K.R. Park, GAN-based blur restoration for finger wrinkle biometrics system, IEEE Access 8 (2020) 49857–49872.
[13] W. Zhong, L. Mao, Y. Ning, Fingerprint image denoising and inpainting using generative adversarial networks, Evol. Intell. 17 (2024) 599–607.
[14] S. Gonzalez-Sabbagh, A. Robles-Kelly, S. Gao, DGD-cGAN: a dual generator for image dewatering and restoration, Pattern Recognit. 148 (2024) 110159.
[15] E. Gavas, A. Namboodiri, Finger-UNet: a U-Net based multi-task architecture for deep fingerprint enhancement, arXiv, 2023.
[16] S. Ojha, N. Kumar, Fingerprint restoration and identification using Pix2Pix cGAN and triplet loss, in: Proc. IEEE Int. Conf. Women Innov, IEEE Int. Conf. Women Innov, 2024, pp. 212–217.
[17] M. Bhilavade, M.R. Patil, K.S. Shivaprakasha, L.S. Admuthe, A.S. Awati, Image inpainting for fingerprint reconstruction, 2023 World Conference on Communication & Computing (WCONF), 2023, pp. 1–6.
[18] Y. Jin, S. Kwak, S. Ham, J. Kim, A fast and efficient numerical algorithm for image segmentation and denoising, AIMS Math. 9 (2) (2024) 5015–5027.
[19] S. Ham, H. Kim, Y. Hwang, S. Kwak, J. Jyoti, H. Wang, W. Xu, J. Jiang, Kim, A novel phase-field model for three-dimensional shape transformation, Comput. Math. Appl. 176 (2024) 67–76.
[20] S. Su, J. Yang, Unconditionally stable algorithm with unique solvability for image inpainting using a penalized Allen-Cahn equation, Commun. Nonlinear Sci. Numer. Simul. 142 (2025) 108503.
[21] J. Wang, Z. Han, J. Kim, An efficient and explicit local image inpainting method using the Allen-Cahn equation, Z. Angew. Math. Phys. 75 (2024) 44.
[22] Q. Xia, G. Sun, J. Kim, Y. Li, Multi-scale modeling and simulation of additive manufacturing based on fused deposition technique, Phys. Fluids 35 (Article 034116) (2023).
[23] Q. Xia, G. Sun, Q. Yu, J. Kim, Y. Li, Thermal-fluid topology optimization with unconditional energy stability and second-order accuracy via phase-field model, Commun. Nonlinear Sci. Numer. Simul. 116 (2023) 106782.
[24] Q. Xia, J. Yang, Y. Li, On the conservative phase-field method with the N-component incompressible flows, Phys. Fluids 35 (Article 012120) (2023).
[25] Y. Li, Q. Xia, C. Lee, S. Kim, J. Kim, A robust and efficient fingerprint image restoration method based on a phase-field model, Pattern Recognit. 123 (2022) 108405.
[26] C. Lee, S. Kim, S. Kwak, Y. Hwang, S. Ham, S. Kang, J. Kim, Semi-automatic fingerprint image restoration algorithm using a partial differential equation, AIMS Math. 8 (11) (2023) 27528–27541.
[27] J. Yang, C. Lee, D. Jeong, J. Kim, A simple and explicit numerical method for the phase-field model for diblock copolymer melts, Comput. Mater. Sci. 205 (2022) 111192.
[28] K. Ji, A.M. Tabrizi, A. Karma, Isotropic finite-difference approximations for phase-field simulations of polycrystalline alloy solidification, J. Comput. Phys. 457 (2022) 111069.
[29] S. Pourghanbar, J. Manafian, M. Ranjbar, A. Aliyeva, Y.S. Gasimov, An efficient alternating direction explicit method for solving a nonlinear partial differential equation, Math. Probl. Eng. 2020 (1) (2020) 9647416.
[30] L. Yang, J. Yang, GPU-accelerated flow simulations on unstructured grids using a multi-colored Gauss-Seidel method, In: Asia-Pac. Int. Symp. Aerosp. Technol. 2023, pp. 657–671.
[31] A. Ahmadi, F. Manganiello, A. Khademi, M.C. Smith, A parallel Jacobi-embedded Gauss-Seidel method, IEEE Trans. Parallel Distrib. Syst. 32 (6) (2021) 1452–1464.
[32] D. Maio, D. Maltoni, R. Cappelli, J.L. Wayman, A.K. Jain, in: FVC2004: Third Fingerprint Verification Competition, Berlin; Heidelberg, Springer, 2004.
[33] D. Maio, D. Maltoni, R. Cappelli, J.L. Wayman, A.K. Jain, FVC2000: Fingerprint verification competition, IEEE Trans. Pattern Anal. Mach. Intell. 24 (2002) 402–412.
[34] D. Maio, D. Maltoni, R. Cappelli, J.L. Wayman, A.K. Jain, Proc. International Conference on Pattern Recognition (ICPR), International Conference on Pattern Recognition (ICPR)Quebec City, Canada, 2002. FVC2002: Second fingerprint verification competition.
[35] P. Qian, A. Li, M. Liu, Latent fingerprint enhancement based on DenseUNet, in: Proc. Int. Conf, Int. Conf, 2019, pp. 1–6.
[36] I. Joshi, A. Anand, S.D. Roy, P.K. Kalra, On training generative adversarial networks for enhancement of latent fingerprints, in Proc. AI Deep Learn. Biometric Secur. 2021, pp. 51–79.
[37] I. Joshi, A. Anand, M. Vatsa, R. Singh, S.D. Roy, P. Kalra, Latent fingerprint enhancement using generative adversarial networks, in: Proc. IEEE Winter Conf. Appl. Comput. Vis, IEEE Winter Conf. Appl. Comput. Vis, 2019, pp. 895–903.
[38] Y. Rao, C. Li, F. Xu, Y. Guo, MSAPVT: A multi-scale attention pyramid vision transformer network for large-scale fruit recognition, J. Food Meas. Charact. 18 (2024) 9233–9251.
[39] M. Khouy, Y. Jabrane, M. Ameur, A.E. Hajjam, Hassani, Medical image segmentation using automatic optimized U-Net architecture based on genetic algorithm, J. Pers. Med. 13 (9) (2023) 1298.
[40] P.K. Rao, S. Singh, A. Dey, D. Rawtani, G. Parikh, Automated fingerprint identification system, in: Modern Forensic Tools and Devices: Trends in Criminal Investigation, Wiley, 2023, pp. 107–124.